Nano Active Stabilization System - Effect of rotation

Dehaeze Thomas

April 3, 2025

Contents

An important aspect of the Nano Active Stabilization System (NASS) is that the nano-hexapod continuously rotates around a vertical axis, whereas the external metrology is not. Such rotation induces gyroscopic effects that may impact the system dynamics and obtained performance. To study these effects, a model of a rotating suspended platform is first presented (Section 1) This model is simple enough to be able to derive its dynamics analytically and to understand its behavior, while still allowing the capture of important physical effects in play.

Integral Force Feedback (IFF) is then applied to the rotating platform, and it is shown that the unconditional stability of IFF is lost due to the gyroscopic effects induced by the rotation (Section 2). Two modifications of the Integral Force Feedback are then proposed. The first modification involves adding a high-pass filter to the IFF controller (Section 3). It is shown that the IFF controller is stable for some gain values, and that damping can be added to the suspension modes. The optimal high-pass filter cut-off frequency is computed. The second modification consists of adding a stiffness in parallel to the force sensors (Section 4). Under certain conditions, the unconditional stability of the IFF controller is regained. The optimal parallel stiffness is then computed. This study of adapting IFF for the damping of rotating platforms has been the subject of two published papers [1], [2].

It is then shown that Relative Damping Control (RDC) is less affected by gyroscopic effects (Section 5). Once the optimal control parameters for the three tested active damping techniques are obtained, they are compared in terms of achievable damping, damped plant and closed-loop compliance and transmissibility (Section 6).

The previous analysis was applied to three considered nano-hexapod stiffnesses ($k_n = 0.01\,N/\mu m$, $k_n = 1\,N/\mu m$ and $k_n = 100\,N/\mu m$) and the optimal active damping controller was obtained in each case (Section 7). Up until this section, the study was performed on a very simplistic model that only captures the rotation aspect, and the model parameters were not tuned to correspond to the NASS. In the last section (Section 8), a model of the micro-station is added below the suspended platform (i.e. the nano-hexapod) with a rotating spindle and parameters tuned to match the NASS dynamics. The goal is to determine whether the rotation imposes performance limitation on the NASS.

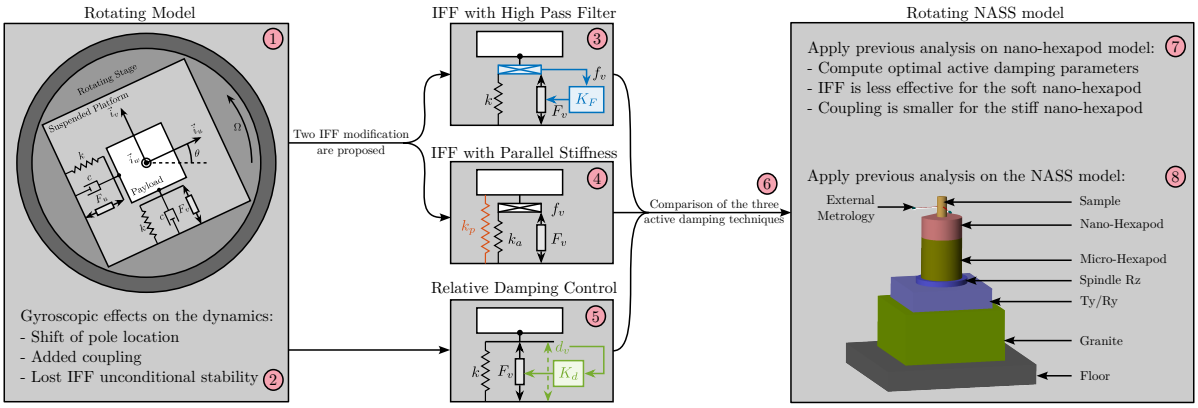

Figure 1: Overview of this chapter's organization. Sections are indicated by the red circles.

1 System Description and Analysis

The system used to study gyroscopic effects consists of a 2 degree of freedom translation stage on top of a rotating stage (Figure 1.1). The rotating stage is supposed to be ideal, meaning it induces a perfect rotation $\theta(t) = \Omega t$ where Ω is the rotational speed in $\mathrm{rad\,s^{-1}}$. The suspended platform consists of two orthogonal actuators, each represented by three elements in parallel: a spring with a stiffness k in $\mathrm{N\,m^{-1}}$, a dashpot with a damping coefficient c in $\mathrm{N/(m/s)}$ and an ideal force source F_u, F_v. A payload with a mass m in kg, is mounted on the (rotating) suspended platform. Two reference frames are used: an *inertial* frame $(\vec{i}_x, \vec{i}_y, \vec{i}_z)$ and a *uniform rotating* frame $(\vec{i}_u, \vec{i}_v, \vec{i}_w)$ rigidly fixed on top of the rotating stage with $\vec{i}_w$ aligned with the rotation axis. The position of the payload is represented by $(d_u, d_v, 0)$ expressed in the rotating frame. After the dynamics of this system is studied, the objective will be to dampen the two suspension modes of the payload while the rotating stage performs a constant rotation.

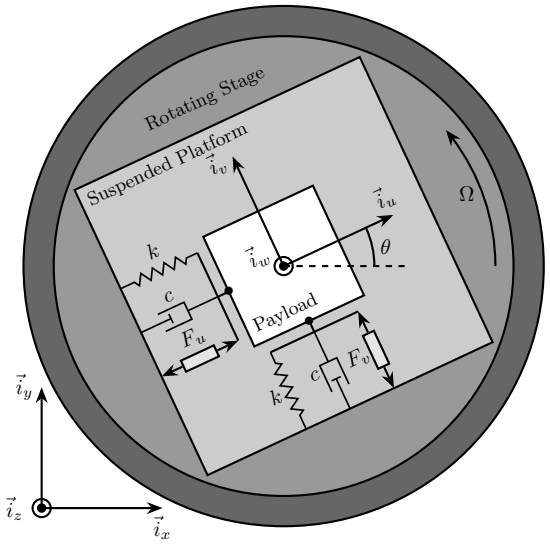

Figure 1.1: Schematic of the studied system

1.1 Equations of motion and transfer functions

To obtain the equations of motion for the system represented in Figure 1.1, the Lagrangian equation (1.1) is used. $L = T - V$ is the Lagrangian, T the kinetic coenergy, V the potential energy, D the dissipation function, and Q_i the generalized force associated with the generalized variable $\begin{bmatrix} q_1 & q_2 \end{bmatrix} = \begin{bmatrix} d_u & d_v \end{bmatrix}$. These terms are derived in (1.2). Note that the equation of motion corresponding to constant rotation along $\vec{i}_w$ is disregarded because this motion is imposed by the rotation stage.

$$\frac{d}{dt}\left(\frac{\partial L}{\partial \dot{q}_i}\right) + \frac{\partial D}{\partial \dot{q}_i} - \frac{\partial L}{\partial q_i} = Q_i \tag{1.1}$$

$$\begin{aligned} T &= \frac{1}{2}m\left((\dot{d}_u - \Omega d_v)^2 + (\dot{d}_v + \Omega d_u)^2\right), \quad Q_1 = F_u, \quad Q_2 = F_v, \\ V &= \frac{1}{2}k\left({d_u}^2 + {d_v}^2\right), \quad D = \frac{1}{2}c\left({\dot{d}_u}^2 + {\dot{d}_v}^2\right) \end{aligned} \tag{1.2}$$

Substituting equations (1.2) into equation (1.1) for both generalized coordinates gives two coupled differential equations (1.3a) and (1.3b).

$$m\ddot{d}_u + c\dot{d}_u + (k - m\Omega^2)d_u = F_u + 2m\Omega\dot{d}_v \tag{1.3a}$$

$$m\ddot{d}_v + c\dot{d}_v + (\underbrace{k - m\Omega^2}_{\text{Centrif.}})d_v = F_v \underbrace{- 2m\Omega\dot{d}_u}_{\text{Coriolis}} \tag{1.3b}$$

The uniform rotation of the system induces two *gyroscopic effects* as shown in equation (1.3):

- *Centrifugal forces*: that can be seen as an added *negative stiffness* $-m\Omega^2$ along $\vec{i}_u$ and $\vec{i}_v$
- *Coriolis forces*: that adds *coupling* between the two orthogonal directions.

One can verify that without rotation ($\Omega = 0$), the system becomes equivalent to two *uncoupled* one degree of freedom mass-spring-damper systems.

To study the dynamics of the system, the two differential equations of motions (1.3) are converted into the Laplace domain and the 2×2 transfer function matrix $\mathbf{G}_d$ from $\begin{bmatrix} F_u & F_v \end{bmatrix}$ to $\begin{bmatrix} d_u & d_v \end{bmatrix}$ in equation (1.4) is obtained. The four transfer functions in $\mathbf{G}_d$ are shown in equation (1.5).

$$\begin{bmatrix} d_u \\ d_v \end{bmatrix} = \mathbf{G}_d \begin{bmatrix} F_u \\ F_v \end{bmatrix} \tag{1.4}$$

$$\mathbf{G}_d(1,1) = \mathbf{G}_d(2,2) = \frac{ms^2 + cs + k - m\Omega^2}{\left(ms^2 + cs + k - m\Omega^2\right)^2 + \left(2m\Omega s\right)^2} \tag{1.5a}$$

$$\mathbf{G}_d(1,2) = -\mathbf{G}_d(2,1) = \frac{2m\Omega s}{\left(ms^2 + cs + k - m\Omega^2\right)^2 + \left(2m\Omega s\right)^2} \tag{1.5b}$$

To simplify the analysis, the undamped natural frequency ω_0 and the damping ratio ξ defined in (1.6) are used instead. The elements of the transfer function matrix $\mathbf{G}_d$ are described by equation (1.7).

$$\omega_0 = \sqrt{\frac{k}{m}} \text{ in } \mathrm{rad\,s^{-1}}, \quad \xi = \frac{c}{2\sqrt{km}} \tag{1.6}$$

$$\mathbf{G}_d(1,1) = \frac{\frac{1}{k}\left(\frac{s^2}{{\omega_0}^2} + 2\xi\frac{s}{\omega_0} + 1 - \frac{\Omega^2}{{\omega_0}^2}\right)}{\left(\frac{s^2}{{\omega_0}^2} + 2\xi\frac{s}{\omega_0} + 1 - \frac{\Omega^2}{{\omega_0}^2}\right)^2 + \left(2\frac{\Omega}{\omega_0}\frac{s}{\omega_0}\right)^2} \tag{1.7a}$$

$$\mathbf{G}_d(1,2) = \frac{\frac{1}{k}\left(2\frac{\Omega}{\omega_0}\frac{s}{\omega_0}\right)}{\left(\frac{s^2}{{\omega_0}^2} + 2\xi\frac{s}{\omega_0} + 1 - \frac{\Omega^2}{{\omega_0}^2}\right)^2 + \left(2\frac{\Omega}{\omega_0}\frac{s}{\omega_0}\right)^2} \tag{1.7b}$$

1.2 System Poles: Campbell Diagram

The poles of $\mathbf{G}_d$ are the complex solutions p of equation (1.8) (i.e. the roots of its denominator).

$$\left(\frac{p^2}{{\omega_0}^2} + 2\xi\frac{p}{\omega_0} + 1 - \frac{\Omega^2}{{\omega_0}^2}\right)^2 + \left(2\frac{\Omega}{\omega_0}\frac{p}{\omega_0}\right)^2 = 0 \tag{1.8}$$

Supposing small damping ($\xi \ll 1$), two pairs of complex conjugate poles $[p_+, p_-]$ are obtained as shown in equation (1.9).

$$p_+ = -\xi\omega_0\left(1 + \frac{\Omega}{\omega_0}\right) \pm j\omega_0\left(1 + \frac{\Omega}{\omega_0}\right) \tag{1.9a}$$

$$p_- = -\xi\omega_0\left(1 - \frac{\Omega}{\omega_0}\right) \pm j\omega_0\left(1 - \frac{\Omega}{\omega_0}\right) \tag{1.9b}$$

The real and complex parts of these two pairs of complex conjugate poles are represented in Figure 1.2 as a function of the rotational speed Ω. As the rotational speed increases, p_+ goes to higher frequencies and p_- goes to lower frequencies (Figure 1.2b). The system becomes unstable for $\Omega > \omega_0$ as the real part of p_- is positive (Figure 1.2a). Physically, the negative stiffness term $-m\Omega^2$ induced by centrifugal forces exceeds the spring stiffness k.

1.3 System Dynamics: Effect of rotation

The system dynamics from actuator forces $[F_u, F_v]$ to the relative motion $[d_u, d_v]$ is identified for several rotating velocities. Looking at the transfer function matrix $\mathbf{G}_d$ in equation (1.7), one can see that the two diagonal (direct) terms are equal and that the two off-diagonal (coupling) terms are opposite. The bode plots of these two terms are shown in Figure 1.3 for several rotational speeds Ω. These plots confirm the expected behavior: the frequencies of the two pairs of complex conjugate poles are further separated as Ω increases. For $\Omega > \omega_0$, the low-frequency pair of complex conjugate poles p_- becomes unstable (shown be the 180 degrees phase lead instead of phase lag).

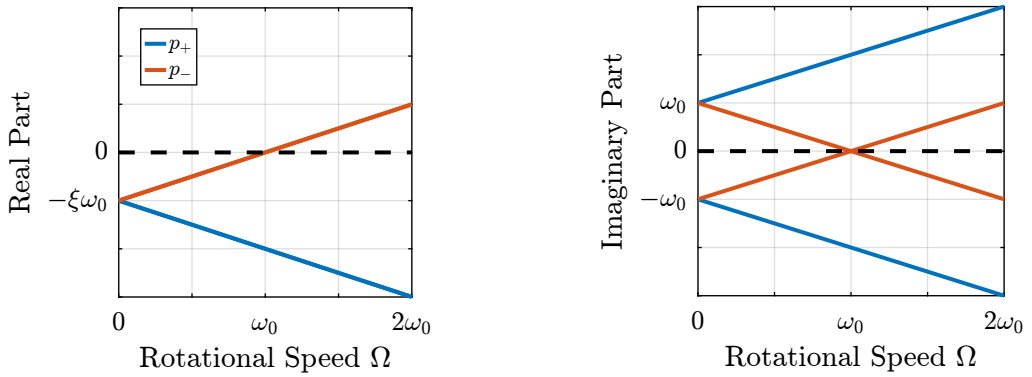

(a) Real part

(b) Imaginary part

Figure 1.2: Campbell diagram - Real (a) and Imaginary (b) parts of the poles as a function of the rotating velocity Ω.

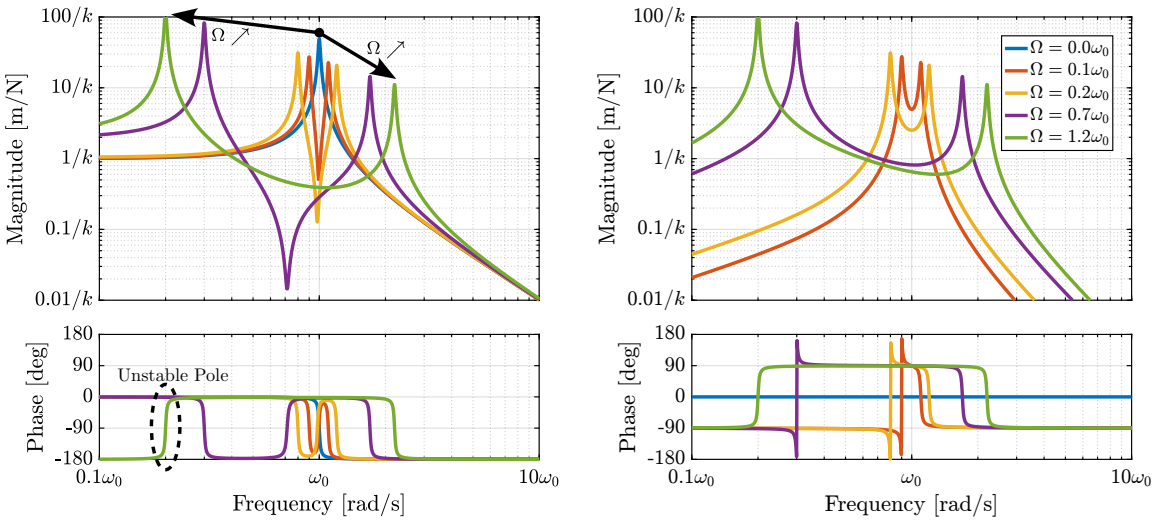

(a) Direct terms: d_u/F_u, d_v/F_v

(b) Coupling terms: d_u/F_v, d_v/F_u

Figure 1.3: Bode plot of the direct (a) and coupling (a) terms for several rotating velocities

2 Integral Force Feedback

The goal is now to damp the two suspension modes of the payload using an active damping strategy while the rotating stage performs a constant rotation. As was explained with the uniaxial model, such an active damping strategy is key to both reducing the magnification of the response in the vicinity of the resonances [3] and to make the plant easier to control for the high authority controller.

Many active damping techniques have been developed over the years, such as Positive Position Feedback (PPF) [4], [5], Integral Force Feedback (IFF) [6] and Direct Velocity Feedback (DVF) [7], [8], [9]. In [6], the IFF control scheme has been proposed, where a force sensor, a force actuator, and an integral controller are used to increase the damping of a mechanical system. When the force sensor is collocated with the actuator, the open-loop transfer function has alternating poles and zeros, which guarantees the stability of the closed-loop system [9]. It was later shown that this property holds for multiple collated actuator/sensor pairs [10].

The main advantages of IFF over other active damping techniques are the guaranteed stability even in the presence of flexible dynamics, good performance, and robustness properties [9].

Several improvements to the classical IFF have been proposed, such as adding a feed-through term to increase the achievable damping [11] or adding a high-pass filter to recover the loss of compliance at low-frequency [12]. Recently, an $\mathcal{H}_\infty$ optimization criterion has been used to derive optimal gains for the IFF controller [13].

However, none of these studies have been applied to rotating systems. In this section, the IFF strategy is applied on the rotating suspended platform, and it is shown that gyroscopic effects alter the system dynamics and that IFF cannot be applied as is.

2.1 System and Equations of motion

To apply Integral Force Feedback, two force sensors are added in series with the actuators (Figure 2.1a). Two identical controllers K_F described by (2.1) are then used to feedback each of the sensed force to its associated actuator.

$$K_F(s) = g \cdot \frac{1}{s} \tag{2.1}$$

The forces $\begin{bmatrix} f_u & f_v \end{bmatrix}$ measured by the two force sensors represented in Figure 2.1a are described by equation (2.2).

$$\begin{bmatrix} f_u \\ f_v \end{bmatrix} = \begin{bmatrix} F_u \\ F_v \end{bmatrix} - (cs + k) \begin{bmatrix} d_u \\ d_v \end{bmatrix} \tag{2.2}$$

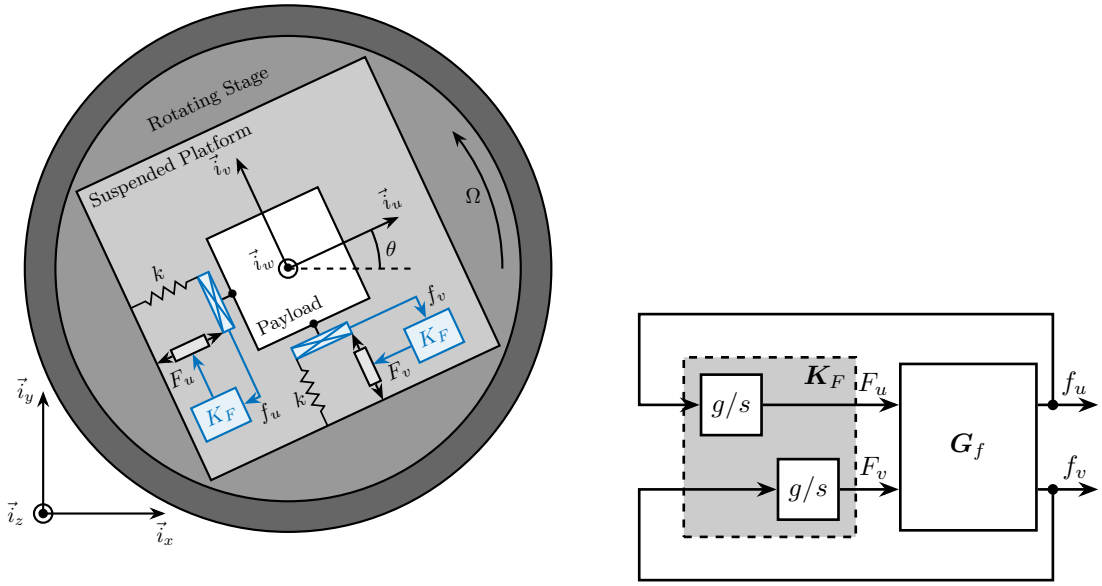

(a) System with added Force Sensor in series with the actuators

(b) Control diagram

Figure 2.1: Integral Force Feedback applied to the suspended rotating platform. The damper c in (a) is omitted for readability.

The transfer function matrix $\mathbf{G}_f$ from actuator forces to measured forces in equation (2.3) can be obtained by inserting equation (1.7) into equation (2.2). Its elements are shown in equation (2.4).

$$\begin{bmatrix} f_u \\ f_v \end{bmatrix} = \mathbf{G}_f \begin{bmatrix} F_u \\ F_v \end{bmatrix} \tag{2.3}$$

$$\mathbf{G}_f(1,1) = \mathbf{G}_f(2,2) = \frac{\left(\frac{s^2}{{\omega_0}^2} - \frac{\Omega^2}{{\omega_0}^2}\right)\left(\frac{s^2}{{\omega_0}^2} + 2\xi\frac{s}{\omega_0} + 1 - \frac{\Omega^2}{{\omega_0}^2}\right) + \left(2\frac{\Omega}{\omega_0}\frac{s}{\omega_0}\right)^2}{\left(\frac{s^2}{{\omega_0}^2} + 2\xi\frac{s}{\omega_0} + 1 - \frac{\Omega^2}{{\omega_0}^2}\right)^2 + \left(2\frac{\Omega}{\omega_0}\frac{s}{\omega_0}\right)^2} \tag{2.4a}$$

$$\mathbf{G}_f(1,2) = -\mathbf{G}_f(2,1) = \frac{-\left(2\xi\frac{s}{\omega_0} + 1\right)\left(2\frac{\Omega}{\omega_0}\frac{s}{\omega_0}\right)}{\left(\frac{s^2}{{\omega_0}^2} + 2\xi\frac{s}{\omega_0} + 1 - \frac{\Omega^2}{{\omega_0}^2}\right)^2 + \left(2\frac{\Omega}{\omega_0}\frac{s}{\omega_0}\right)^2} \tag{2.4b}$$

The zeros of the diagonal terms of $\mathbf{G}_f$ in equation (2.4a) are computed, and neglecting the damping for simplicity, two complex conjugated zeros z_c (2.5a), and two real zeros z_r (2.5b) are obtained.

$$z_c = \pm j\omega_0\sqrt{\frac{1}{2}\sqrt{8\frac{\Omega^2}{{\omega_0}^2} + 1} + \frac{\Omega^2}{{\omega_0}^2} + \frac{1}{2}} \tag{2.5a}$$

$$z_r = \pm\omega_0\sqrt{\frac{1}{2}\sqrt{8\frac{\Omega^2}{{\omega_0}^2} + 1} - \frac{\Omega^2}{{\omega_0}^2} - \frac{1}{2}} \tag{2.5b}$$

It is interesting to see that the frequency of the pair of complex conjugate zeros z_c in equation (2.5a) always lies between the frequency of the two pairs of complex conjugate poles p_- and p_+ in equation (1.9). This is what usually gives the unconditional stability of IFF when collocated force sensors are used.

However, for non-null rotational speeds, the two real zeros z_r in equation (2.5b) are inducing a *non-minimum phase behavior*. This can be seen in the Bode plot of the diagonal terms (Figure 2.2) where the low-frequency gain is no longer zero while the phase stays at 180°.

The low-frequency gain of $\mathbf{G}_f$ increases with the rotational speed Ω as shown in equation (2.6). This can be explained as follows: a constant actuator force F_u induces a small displacement of the mass $d_u = \frac{F_u}{k - m\Omega^2}$ (Hooke's law considering the negative stiffness induced by the rotation). This small displacement then increases the centrifugal force $m\Omega^2 d_u = \frac{\Omega^2}{{\omega_0}^2 - \Omega^2} F_u$ which is then measured by the force sensors.

$$\lim_{\omega \to 0} |\mathbf{G}_f(j\omega)| = \begin{bmatrix} \frac{\Omega^2}{{\omega_0}^2 - \Omega^2} & 0 \\ 0 & \frac{\Omega^2}{{\omega_0}^2 - \Omega^2} \end{bmatrix} \tag{2.6}$$

2.2 Effect of rotation speed on IFF plant dynamics

The transfer functions from actuator forces $[F_u,\ F_v]$ to the measured force sensors $[f_u,\ f_v]$ are identified for several rotating velocities and are shown in Figure 2.2. As expected from the derived equations of motion:

- when $\Omega < \omega_0$: the low-frequency gain is no longer zero and two (non-minimum phase) real zeros appear at low-frequencies. The low-frequency gain increases with Ω. A pair of (minimum phase) complex conjugate zeros appears between the two complex conjugate poles, which are split further apart as Ω increases.
- when $\omega_0 < \Omega$: the low-frequency pole becomes unstable.

2.3 Decentralized Integral Force Feedback

The control diagram for decentralized IFF is shown in Figure 2.1b. The decentralized IFF controller $\boldsymbol{K}_F$ corresponds to a diagonal controller with integrators (2.7).

$$\begin{aligned} \mathbf{K}_F(s) &= \begin{bmatrix} K_F(s) & 0 \\ 0 & K_F(s) \end{bmatrix} \\ K_F(s) &= g \cdot \frac{1}{s} \end{aligned} \tag{2.7}$$

To determine how the IFF controller affects the poles of the closed-loop system, a Root Locus plot (Figure 2.2b) is constructed as follows: the poles of the closed-loop system are drawn in the complex plane as the controller gain g varies from 0 to ∞ for the two controllers K_F simultaneously. As explained

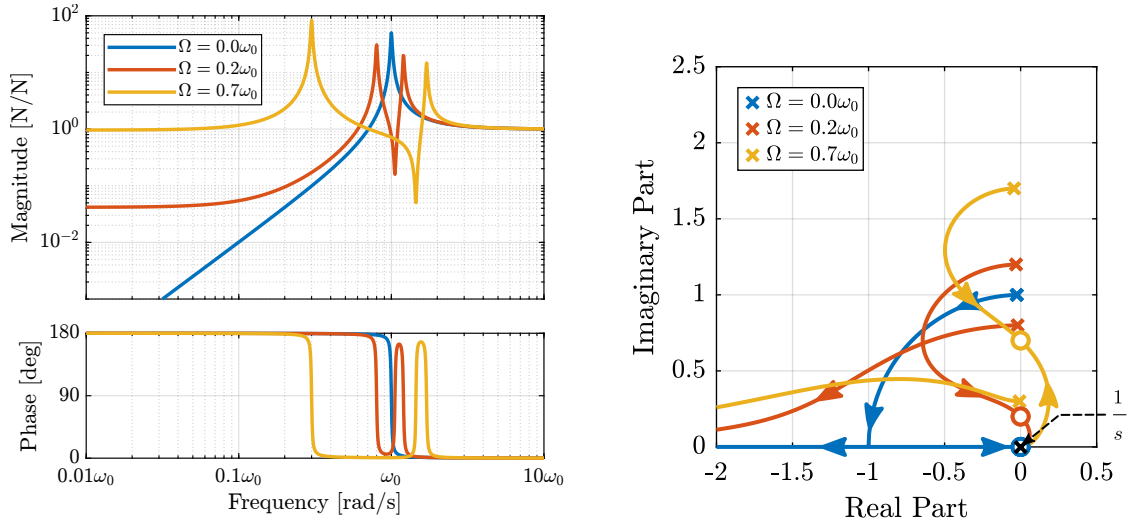

(a) Direct terms: d_u/F_u, d_v/F_v

(b) Root Locus

Figure 2.2: Effect of the rotation velocity on the bode plot of the direct terms (a) and on the IFF root locus (b)

in [10], [14], the closed-loop poles start at the open-loop poles (shown by ✖) for $g = 0$ and coincide with the transmission zeros (shown by ⭘) as $g \to \infty$.

Whereas collocated IFF is usually associated with unconditional stability [6], this property is lost due to gyroscopic effects as soon as the rotation velocity becomes non-null. This can be seen in the Root Locus plot (Figure 2.2b) where poles corresponding to the controller are bound to the right half plane implying closed-loop system instability. Physically, this can be explained as follows: at low frequencies, the loop gain is huge due to the pure integrator in K_F and the finite gain of the plant (Figure 2.2). The control system is thus cancels the spring forces, which makes the suspended platform not capable to hold the payload against centrifugal forces, hence the instability.

3 Integral Force Feedback with a High-Pass Filter

As explained in the previous section, the instability of the IFF controller applied to the rotating system is due to the high gain of the integrator at low-frequency. To limit the low-frequency controller gain, a high-pass filter (HPF) can be added to the controller, as shown in equation (3.1). This is equivalent to slightly shifting the controller pole to the left along the real axis. This modification of the IFF controller is typically performed to avoid saturation associated with the pure integrator [6], [15]. This is however not the reason why this high-pass filter is added here.

$$\boxed{K_F(s) = g \cdot \frac{1}{s} \cdot \underbrace{\frac{s/\omega_i}{1 + s/\omega_i}}_{\text{HPF}} = g \cdot \frac{1}{s + \omega_i}} \tag{3.1}$$

3.1 Modified Integral Force Feedback Controller

The Integral Force Feedback Controller is modified such that instead of using pure integrators, pseudo integrators (i.e. low pass filters) are used (3.1) where ω_i characterize the frequency down to which the signal is integrated. The loop gains ($K_F(s)$ times the direct dynamics f_u/F_u) with and without the added HPF are shown in Figure 3.1a. The effect of the added HPF limits the low-frequency gain to finite values as expected.

The Root Locus plots for the decentralized IFF with and without the HPF are displayed in Figure 3.1b. With the added HPF, the poles of the closed-loop system are shown to be stable up to some value of the gain $g_{\max}$ given by equation (3.2). It is interesting to note that $g_{\max}$ also corresponds to the controller gain at which the low-frequency loop gain reaches one (for instance the gain g can be increased by a factor 5 in Figure 3.1a before the system becomes unstable).

$$\boxed{g_{\max} = \omega_i \left(\frac{{\omega_0}^2}{\Omega^2} - 1 \right)} \tag{3.2}$$

3.2 Optimal IFF with HPF parameters ω_i and g

Two parameters can be tuned for the modified controller in equation (3.1): the gain g and the pole's location ω_i. The optimal values of ω_i and g are considered here as the values for which the damping of all the closed-loop poles is simultaneously maximized.

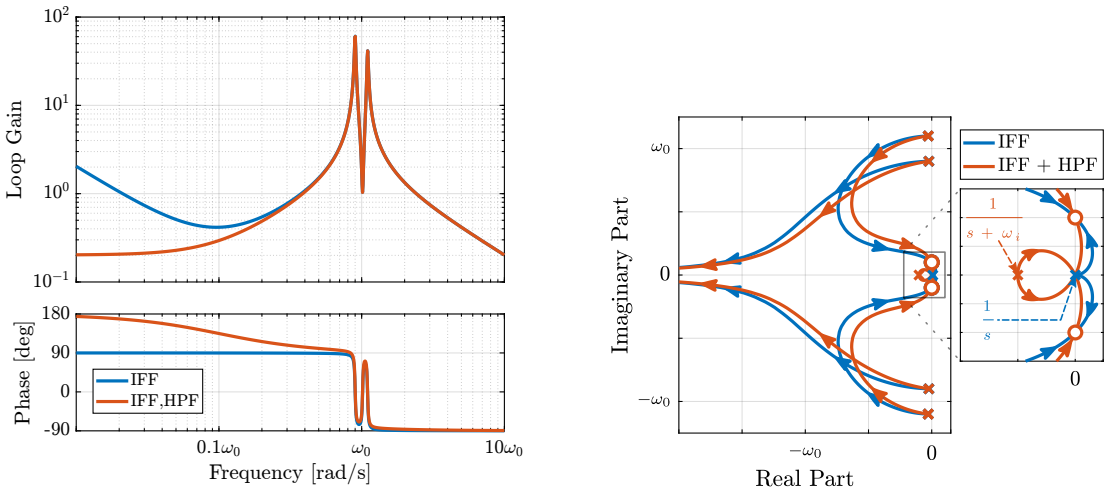

(a) Loop gain

(b) Root Locus

Figure 3.1: Comparison of the IFF with pure integrator and modified IFF with added high-pass filter ($\Omega = 0.1\omega_0$). The loop gain is shown in (a) with $\omega_i = 0.1\omega_0$ and $g = 2$. The root locus is shown in (b)

To visualize how ω_i does affect the attainable damping, the Root Locus plots for several ω_i are displayed in Figure 3.2a. It is shown that even though small ω_i seem to allow more damping to be added to the suspension modes (see Root locus in Figure 3.2a), the control gain g may be limited to small values due to equation (3.2). To study this trade-off, the attainable closed-loop damping ratio ξ_{cl} is computed as a function of ω_i/ω_0. The gain g_{opt} at which this maximum damping is obtained is also displayed and compared with the gain $g_{\max}$ at which the system becomes unstable (Figure 3.2b).

For small values of ω_i, the added damping is limited by the maximum allowed control gain $g_{\max}$ (red curve and dashed red curve superimposed in Figure 3.2b) at which point the pole corresponding to the controller becomes unstable. For larger values of ω_i, the attainable damping ratio decreases as a function of ω_i as was predicted from the root locus plot of Figure 3.1b.

3.3 Obtained Damped Plant

To study how the parameter ω_i affects the damped plant, the obtained damped plants for several ω_i are compared in Figure 3.3a. It can be seen that the low-frequency coupling increases as ω_i increases. Therefore, there is a trade-off between achievable damping and added coupling when tuning ω_i. The same trade-off can be seen between achievable damping and loss of compliance at low-frequency (see Figure 3.3b).

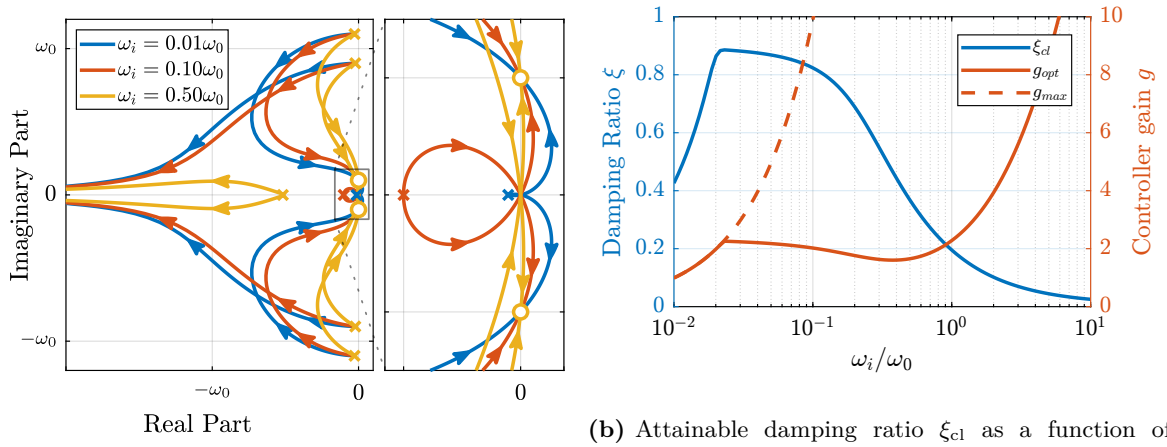

(a) Root Locus

(b) Attainable damping ratio ξ_{cl} as a function of ω_i/ω_0. Corresponding control gain g_{opt} and $g_{\max}$ are also shown

Figure 3.2: Root Locus for several high-pass filter cut-off frequency (a). The achievable damping ratio decreases as ω_i increases, as confirmed in (b)

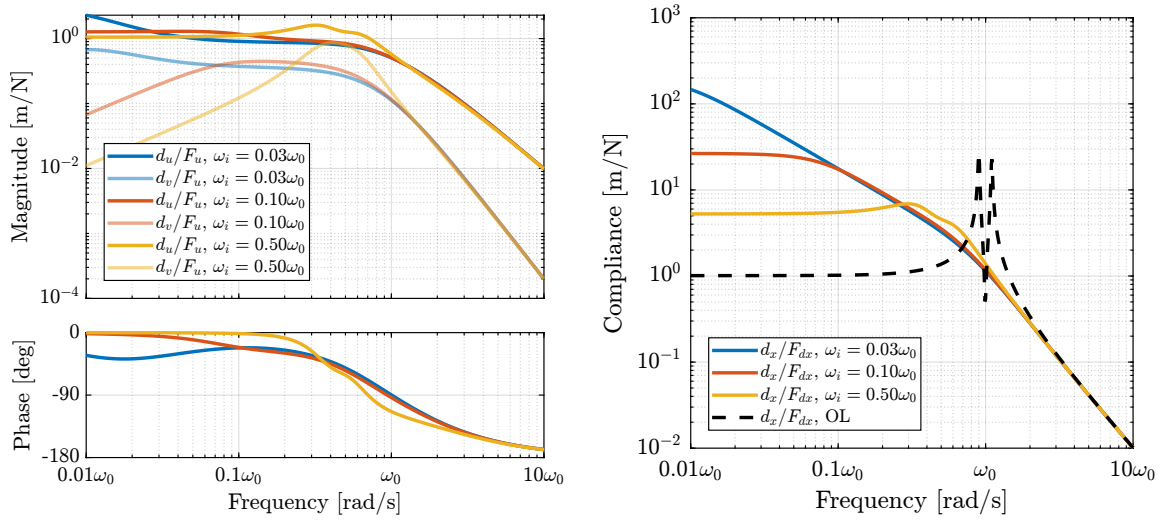

(a) Obtained plants

(b) Effect of ω_i on the compliance

Figure 3.3: Effect of ω_i on the damped plant coupling

4 IFF with a stiffness in parallel with the force sensor

In this section it is proposed to add springs in parallel with the force sensors to counteract the negative stiffness induced by the gyroscopic effects. Such springs are schematically shown in Figure 4.1 where k_a is the stiffness of the actuator and k_p the added stiffness in parallel with the actuator and force sensor.

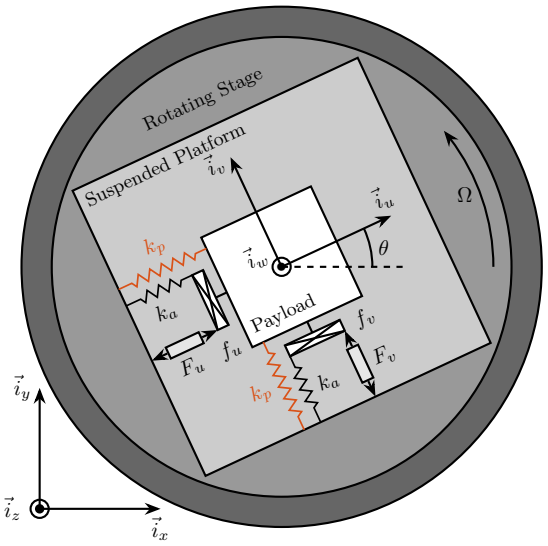

Figure 4.1: Studied system with additional springs in parallel with the actuators and force sensors (shown in red)

4.1 Equations

The forces measured by the two force sensors represented in Figure 4.1 are described by (4.1).

$$\begin{bmatrix} f_u \\ f_v \end{bmatrix} = \begin{bmatrix} F_u \\ F_v \end{bmatrix} - (cs + k_a) \begin{bmatrix} d_u \\ d_v \end{bmatrix} \tag{4.1}$$

To keep the overall stiffness $k = k_a + k_p$ constant, thus not modifying the open-loop poles as k_p is changed, a scalar parameter α ($0 \leq \alpha < 1$) is defined to describe the fraction of the total stiffness in parallel with the actuator and force sensor as in (4.2).

$$k_p = \alpha k, \quad k_a = (1-\alpha)k \tag{4.2}$$

After the equations of motion are derived and transformed in the Laplace domain, the transfer function matrix $\mathbf{G}_k$ in Eq. (4.3) is computed. Its elements are shown in Eqs. (4.4a) and (4.4b).

$$\begin{bmatrix} f_u \\ f_v \end{bmatrix} = \mathbf{G}_k \begin{bmatrix} F_u \\ F_v \end{bmatrix} \tag{4.3}$$

$$\mathbf{G}_k(1,1) = \mathbf{G}_k(2,2) = \frac{\left(\frac{s^2}{{\omega_0}^2} - \frac{\Omega^2}{{\omega_0}^2} + \alpha\right)\left(\frac{s^2}{{\omega_0}^2} + 2\xi\frac{s}{\omega_0} + 1 - \frac{\Omega^2}{{\omega_0}^2}\right) + \left(2\frac{\Omega}{\omega_0}\frac{s}{\omega_0}\right)^2}{\left(\frac{s^2}{{\omega_0}^2} + 2\xi\frac{s}{\omega_0} + 1 - \frac{\Omega^2}{{\omega_0}^2}\right)^2 + \left(2\frac{\Omega}{\omega_0}\frac{s}{\omega_0}\right)^2} \tag{4.4a}$$

$$\mathbf{G}_k(1,2) = -\mathbf{G}_k(2,1) = \frac{-\left(2\xi\frac{s}{\omega_0} + 1 - \alpha\right)\left(2\frac{\Omega}{\omega_0}\frac{s}{\omega_0}\right)}{\left(\frac{s^2}{{\omega_0}^2} + 2\xi\frac{s}{\omega_0} + 1 - \frac{\Omega^2}{{\omega_0}^2}\right)^2 + \left(2\frac{\Omega}{\omega_0}\frac{s}{\omega_0}\right)^2} \tag{4.4b}$$

Comparing $\mathbf{G}_k$ in (4.4) with $\mathbf{G}_f$ in (2.4) shows that while the poles of the system remain the same, the zeros of the diagonal terms change. The two real zeros z_r in (2.5b) that were inducing a non-minimum phase behavior are transformed into two complex conjugate zeros if the condition in (4.5) holds. Thus, if the added *parallel stiffness* k_p is higher than the *negative stiffness* induced by centrifugal forces $m\Omega^2$, the dynamics from the actuator to its collocated force sensor will show *minimum phase behavior*.

$$\boxed{\alpha > \frac{\Omega^2}{{\omega_0}^2} \quad \Leftrightarrow \quad k_p > m\Omega^2} \tag{4.5}$$

4.2 Effect of parallel stiffness on the IFF plant

The IFF plant (transfer function from $[F_u, F_v]$ to $[f_u, f_v]$) is identified without parallel stiffness $k_p = 0$, with a small parallel stiffness $k_p < m\Omega^2$ and with a large parallel stiffness $k_p > m\Omega^2$. Bode plots of the obtained dynamics are shown in Figure 4.2a. The two real zeros for $k_p < m\Omega^2$ are transformed into two complex conjugate zeros for $k_p > m\Omega^2$. In that case, the system shows alternating complex conjugate poles and zeros as what is the case in the non-rotating case.

Figure 4.2b shows the Root Locus plots for $k_p = 0$, $k_p < m\Omega^2$ and $k_p > m\Omega^2$ when K_F is a pure integrator, as shown in Eq. (2.7). It is shown that if the added stiffness is higher than the maximum negative stiffness, the poles of the closed-loop system are bounded on the (stable) left half-plane, and hence the unconditional stability of IFF is recovered.

4.3 Effect of k_p on the attainable damping

Even though the parallel stiffness k_p has no impact on the open-loop poles (as the overall stiffness k is kept constant), it has a large impact on the transmission zeros. Moreover, as the attainable damping is

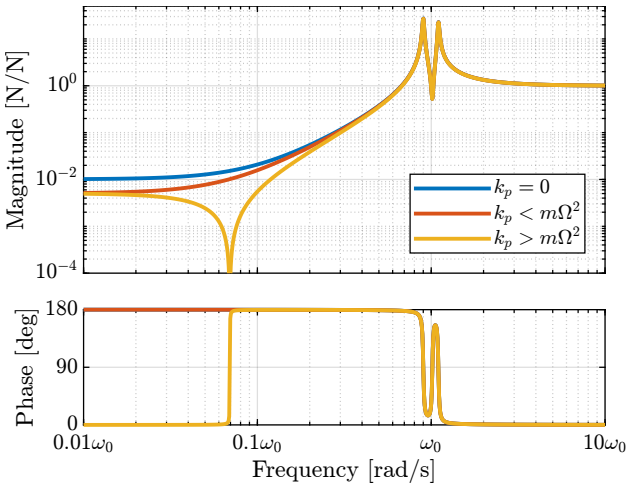

(a) Bode plot of $G_k(1,1) = f_u/F_u$ without parallel spring, with parallel spring stiffness $k_p < m\Omega^2$ and $k_p > m\Omega^2$, $\Omega = 0.1\omega_0$

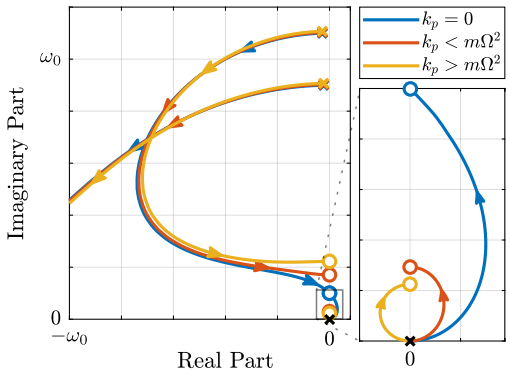

(b) Root Locus for IFF without parallel spring, with small parallel spring and with large parallel spring

Figure 4.2: Effect of parallel stiffness on the IFF plant

generally proportional to the distance between poles and zeros [16], the parallel stiffness k_p is expected to have some impact on the attainable damping. To study this effect, Root Locus plots for several parallel stiffnesses $k_p > m\Omega^2$ are shown in Figure 4.3a. The frequencies of the transmission zeros of the system increase with an increase in the parallel stiffness k_p (thus getting closer to the poles), and the associated attainable damping is reduced. Therefore, even though the parallel stiffness k_p should be larger than $m\Omega^2$ for stability reasons, it should not be taken too large as this would limit the attainable damping. This is confirmed by the Figure 4.3b where the attainable closed-loop damping ratio ξ_{cl} and the associated optimal control gain g_{opt} are computed as a function of the parallel stiffness.

4.4 Damped plant

The parallel stiffness are chosen to be $k_p = 2m\Omega^2$ and the damped plant is computed. The damped and undamped transfer functions from F_u to d_u are compared in Figure 4.4b. Even though the two resonances are well damped, the IFF changes the low-frequency behavior of the plant, which is usually not desired. This is because "pure" integrators are used which are inducing large low-frequency loop gains.

To lower the low-frequency gain, a high-pass filter is added to the IFF controller (which is equivalent as shifting the controller pole to the left in the complex plane):

$$K_{\text{IFF}}(s) = g\frac{1}{\omega_i + s}\begin{bmatrix} 1 & 0 \\ 0 & 1 \end{bmatrix} \tag{4.6}$$

To determine how the high-pass filter impacts the attainable damping, the controller gain g is kept constant while ω_i is changed, and the minimum damping ratio of the damped plant is computed. The obtained damping ratio as a function of ω_i/ω_0 (where ω_0 is the resonance of the system without rotation) is shown in Figure 4.4a. It is shown that the attainable damping ratio reduces as ω_i is increased (same

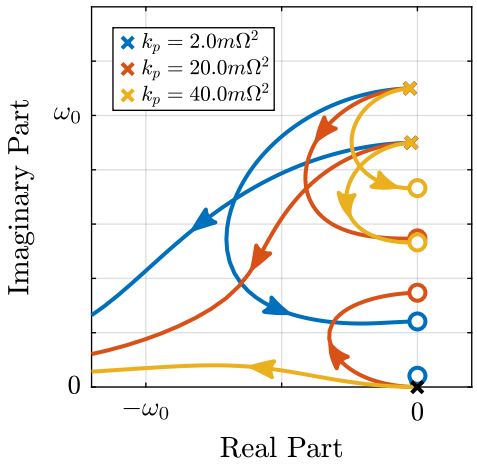

(a) Root Locus: Effect of parallel stiffness on the attainable damping, $\Omega = 0.1\omega_0$

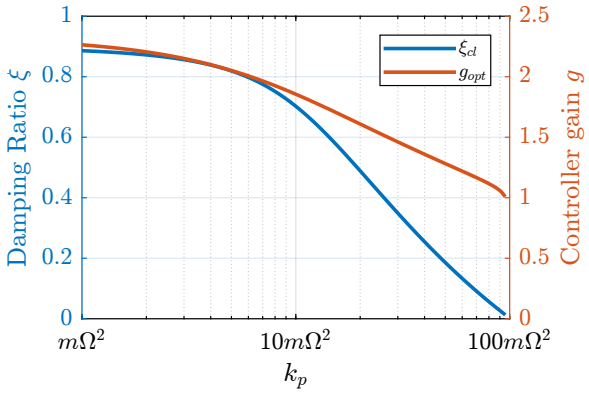

(b) Attainable damping ratio ξ_{cl} as a function of the parallel stiffness k_p. The corresponding control gain g_{opt} is also shown. Values for $k_p < m\Omega^2$ are not shown because the system is unstable.

Figure 4.3: Effect of parallel stiffness on the IFF plant

conclusion than in Section 3). Let's choose $\omega_i = 0.1 \cdot \omega_0$ and compare the obtained damped plant again with the undamped and with the "pure" IFF in Figure 4.4b. The added high-pass filter gives almost the same damping properties to the suspension while exhibiting good low-frequency behavior.

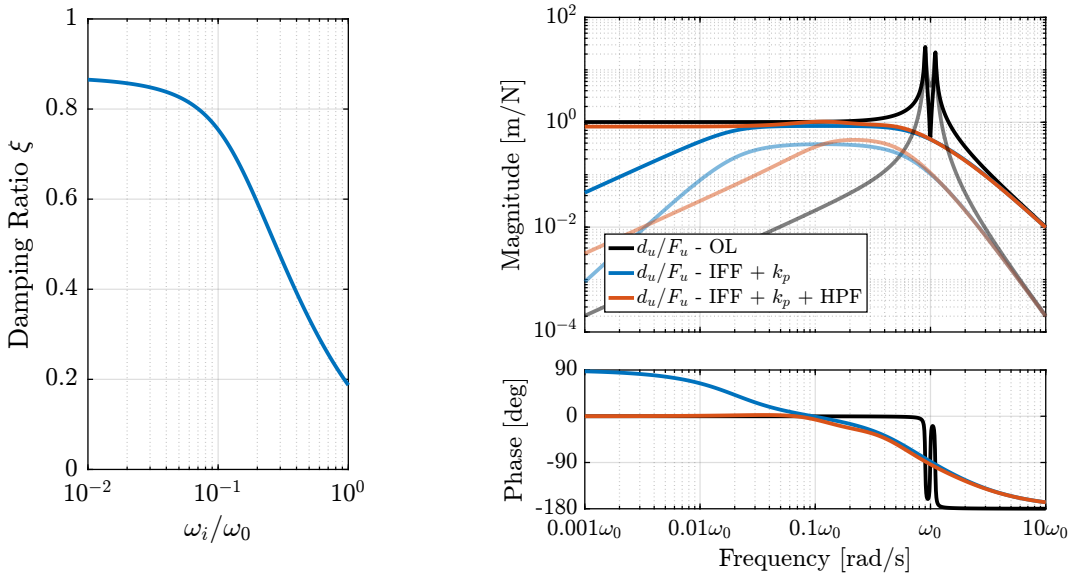

(a) Reduced damping ratio with increased cut-off frequency ω_i

(b) Damped plant with the parallel stiffness, effect of the added HPF

Figure 4.4: Effect of high-pass filter cut-off frequency on the obtained damping

5 Relative Damping Control

To apply a "Relative Damping Control" strategy, relative motion sensors are added in parallel with the actuators as shown in Figure 5.1. Two controllers K_d are used to feed back the relative motion to the actuator. These controllers are in principle pure derivators ($K_d = s$), but to be implemented in practice they are usually replaced by a high-pass filter (5.1).

$$K_d(s) = g \cdot \frac{s}{s + \omega_d} \tag{5.1}$$

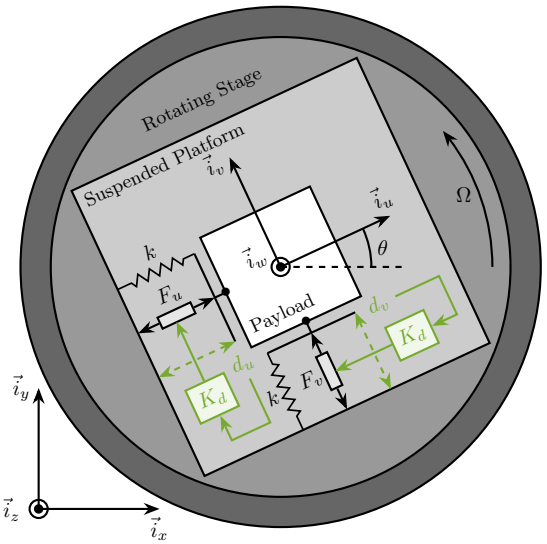

Figure 5.1: System with relative motion sensor and decentralized "relative damping control" applied.

5.1 Equations of motion

Let's note $\boldsymbol{G}_d$ the transfer function between actuator forces and measured relative motion in parallel with the actuators (5.2). The elements of $\boldsymbol{G}_d$ were derived in Section 1 are shown in (5.3).

$$\begin{bmatrix} d_u \\ d_v \end{bmatrix} = \mathbf{G}_d \begin{bmatrix} F_u \\ F_v \end{bmatrix} \tag{5.2}$$

$$\mathbf{G}_d(1,1) = \mathbf{G}_d(2,2) = \frac{\frac{1}{k}\left(\frac{s^2}{{\omega_0}^2} + 2\xi\frac{s}{\omega_0} + 1 - \frac{\Omega^2}{{\omega_0}^2}\right)}{\left(\frac{s^2}{{\omega_0}^2} + 2\xi\frac{s}{\omega_0} + 1 - \frac{\Omega^2}{{\omega_0}^2}\right)^2 + \left(2\frac{\Omega}{\omega_0}\frac{s}{\omega_0}\right)^2} \tag{5.3a}$$

$$\mathbf{G}_d(1,2) = -\mathbf{G}_d(2,1) = \frac{\frac{1}{k}\left(2\frac{\Omega}{\omega_0}\frac{s}{\omega_0}\right)}{\left(\frac{s^2}{{\omega_0}^2} + 2\xi\frac{s}{\omega_0} + 1 - \frac{\Omega^2}{{\omega_0}^2}\right)^2 + \left(2\frac{\Omega}{\omega_0}\frac{s}{\omega_0}\right)^2} \tag{5.3b}$$

Neglecting the damping for simplicity ($\xi \ll 1$), the direct terms have two complex conjugate zeros between the two pairs of complex conjugate poles (5.4). Therefore, for $\Omega < \sqrt{k/m}$ (i.e. stable system), the transfer functions for Relative Damping Control have alternating complex conjugate poles and zeros.

$$z = \pm j\sqrt{\omega_0^2 - \omega^2}, \quad p_1 = \pm j(\omega_0 - \omega), \quad p_2 = \pm j(\omega_0 + \omega) \tag{5.4}$$

5.2 Decentralized Relative Damping Control

The transfer functions from $[F_u,\ F_v]$ to $[d_u,\ d_v]$ were identified for several rotating velocities in Section 1 and are shown in Figure 1.3 (page 7).

To see if large damping can be added with Relative Damping Control, the root locus is computed (Figure 5.2a). The closed-loop system is unconditionally stable as expected and the poles can be damped as much as desired.

Let us select a reasonable "Relative Damping Control" gain, and compute the closed-loop damped system. The open-loop and damped plants are compared in Figure 5.2b. The rotating aspect does not add any complexity to the use of Relative Damping Control. It does not increase the low-frequency coupling as compared to the Integral Force Feedback.

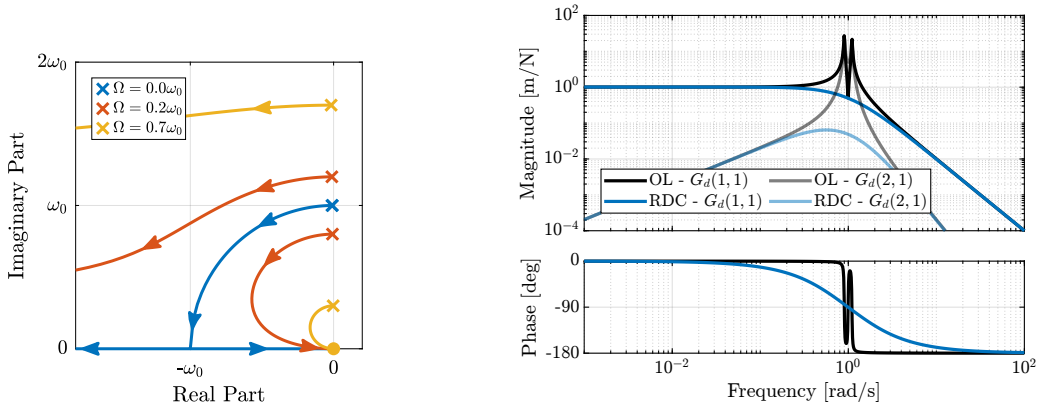

(a) Root Locus for Relative Damping Control **(b)** Damped plant using Relative Damping Control

Figure 5.2: Relative Damping Control. Root Locus (a) and obtained damped plant (b)

6 Comparison of Active Damping Techniques

These two proposed IFF modifications and relative damping control are compared in terms of added damping and closed-loop behavior. For the following comparisons, the cut-off frequency for the added HPF is set to $\omega_i = 0.1\omega_0$ and the stiffness of the parallel springs is set to $k_p = 5m\Omega^2$ (corresponding to $\alpha = 0.05$). These values are chosen one the basis of previous discussions about optimal parameters.

6.1 Root Locus

Figure 6.1a shows the Root Locus plots for the two proposed IFF modifications and the relative damping control. While the two pairs of complex conjugate open-loop poles are identical for both IFF modifications, the transmission zeros are not. This means that the closed-loop behavior of both systems will differ when large control gains are used.

The closed-loop poles corresponding to the system with added springs (in red) are bounded to the left half plane implying unconditional stability. This is not the case for the system in which the controller is augmented with an HPF (in blue). It is interesting to note that the maximum added damping is very similar for both modified IFF techniques.

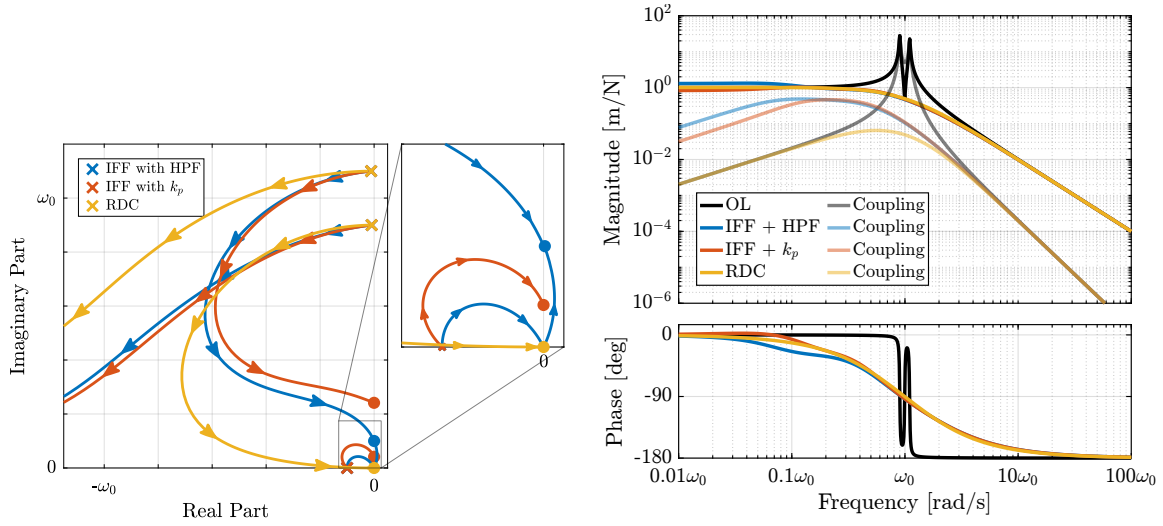

(a) Root Locus

(b) Damped plants

Figure 6.1: Comparison of active damping techniques for rotating platform

6.2 Obtained Damped Plant

The actively damped plants are computed for the three techniques and compared in Figure 6.1b. It is shown that while the diagonal (direct) terms of the damped plants are similar for the three active damping techniques, the off-diagonal (coupling) terms are not. The IFF strategy is adding some coupling at low-frequency, which may negatively impact the positioning performance.

6.3 Transmissibility And Compliance

The proposed active damping techniques are now compared in terms of closed-loop transmissibility and compliance. The transmissibility is defined as the transfer function from the displacement of the rotating stage along $\vec{i}_x$ to the displacement of the payload along the same direction. It is used to characterize the amount of vibration is transmitted through the suspended platform to the payload. The compliance describes the displacement response of the payload to the external forces applied to it. This is a useful metric when disturbances are directly applied to the payload. Here, it is defined as the transfer function from external forces applied on the payload along $\vec{i}_x$ to the displacement of the payload along the same direction.

Very similar results were obtained for the two proposed IFF modifications in terms of transmissibility and compliance (Figure 6.2). Using IFF degrades the compliance at low frequencies, whereas using relative damping control degrades the transmissibility at high frequencies. This is very well known characteristics of these common active damping techniques that hold when applied to rotating platforms.

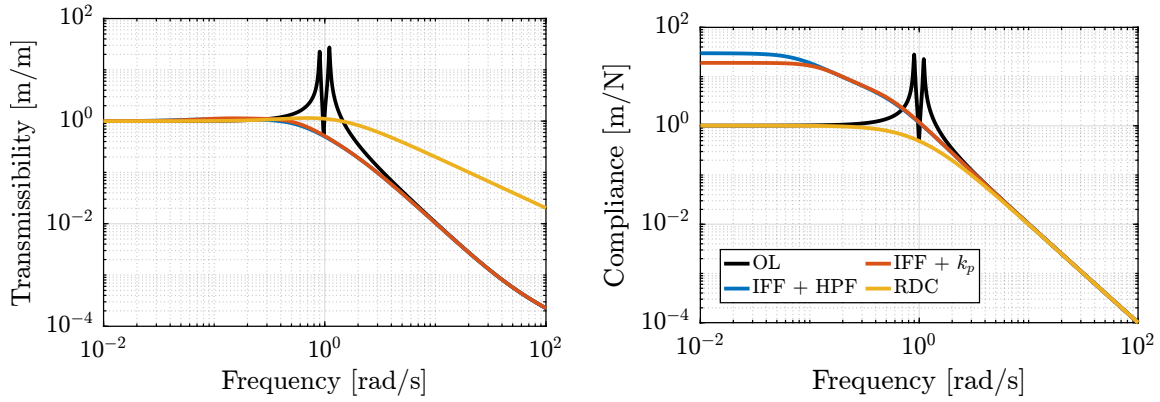

(a) Transmissibility

(b) Compliance

Figure 6.2: Comparison of the obtained transmissibility (a) and compliance (b) for the three tested active damping techniques

7 Rotating Nano-Hexapod

The previous analysis is now applied to a model representing a rotating nano-hexapod. Three nano-hexapod stiffnesses are tested as for the uniaxial model: $k_n = 0.01\,\text{N}/\mu\text{m}$, $k_n = 1\,\text{N}/\mu\text{m}$ and $k_n = 100\,\text{N}/\mu\text{m}$. Only the maximum rotating velocity is here considered ($\Omega = 60\,\text{rpm}$) with the light sample ($m_s = 1\,\text{kg}$) because this is the worst identified case scenario in terms of gyroscopic effects.

7.1 Nano-Active-Stabilization-System - Plant Dynamics

For the NASS, the maximum rotating velocity is $\Omega = 2\pi\,\text{rad}\,\text{s}^{-1}$ for a suspended mass on top of the nano-hexapod's actuators equal to $m_n + m_s = 16\,\text{kg}$. The parallel stiffness corresponding to the centrifugal forces is $m\Omega^2 \approx 0.6\,\text{N}\,\text{mm}^{-1}$.

The transfer functions from the nano-hexapod actuator force F_u to the displacement of the nano-hexapod in the same direction d_u as well as in the orthogonal direction d_v (coupling) are shown in Figure 7.1 for all three considered nano-hexapod stiffnesses. The soft nano-hexapod is the most affected by rotation. This can be seen by the large shift of the resonance frequencies, and by the induced coupling, which is larger than that for the stiffer nano-hexapods. The coupling (or interaction) in a MIMO 2×2 system can be visually estimated as the ratio between the diagonal term and the off-diagonal terms (see corresponding Appendix).

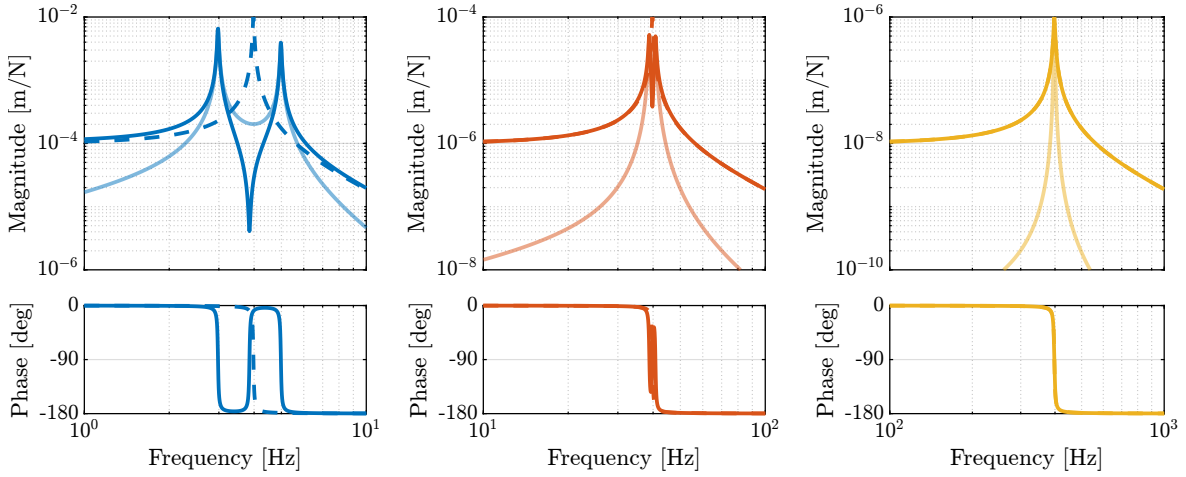

(a) $k_n = 0.01\,N/\mu m$ **(b)** $k_n = 1\,N/\mu m$ **(c)** $k_n = 100\,N/\mu m$

Figure 7.1: Effect of rotation on the nano-hexapod dynamics. Dashed lines represent plants without rotation, solid lines represent plants at maximum rotating velocity ($\Omega = 60\,\text{rpm}$), and shaded lines are coupling terms at maximum rotating velocity

7.2 Optimal IFF with a High-Pass Filter

Integral Force Feedback with an added high-pass filter is applied to the three nano-hexapods. First, the parameters (ω_i and g) of the IFF controller that yield the best simultaneous damping are determined from Figure 7.2. The IFF parameters are chosen as follows:

- for $k_n = 0.01\,\text{N}/\mu\text{m}$ (Figure 7.2): ω_i is chosen such that maximum damping is achieved while the gain is less than half of the maximum gain at which the system is unstable. This is done to have some control robustness.

- for $k_n = 1\,\text{N}/\mu\text{m}$ and $k_n = 100\,\text{N}/\mu\text{m}$ (Figure 7.2b and 7.2c): the largest ω_i is chosen such that the obtained damping is 95 % of the maximum achievable damping. Large ω_i is chosen here to limit the loss of compliance and the increase of coupling at low-frequency as shown in Section 3.

The obtained IFF parameters and the achievable damping are visually shown by large dots in Figure 7.2 and are summarized in Table 7.1.

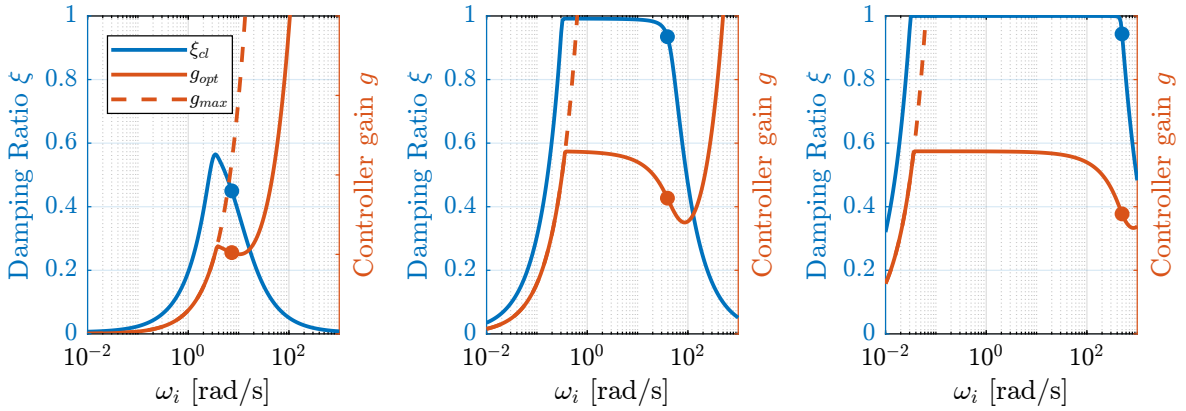

(a) $k_n = 0.01\,N/\mu m$ **(b)** $k_n = 1\,N/\mu m$ **(c)** $k_n = 100\,N/\mu m$

Figure 7.2: For each value of ω_i, the maximum damping ratio ξ is computed (blue), and the corresponding controller gain is shown (in red). The chosen controller parameters used for further analysis are indicated by the large dots.

Table 7.1: Obtained optimal parameters (ω_i and g) for the modified IFF controller including a high-pass filter. The corresponding achievable simultaneous damping of the two modes ξ is also shown.

k_n	ω_i	g	ξ_{opt}
$0.01\,N/\mu m$	7.3	51	0.45
$1\,N/\mu m$	39	427	0.93
$100\,N/\mu m$	500	3775	0.94

7.3 Optimal IFF with Parallel Stiffness

For each considered nano-hexapod stiffness, the parallel stiffness k_p is varied from $k_{p,\min} = m\Omega^2$ (the minimum stiffness that yields unconditional stability) to $k_{p,\max} = k_n$ (the total nano-hexapod stiffness). To keep the overall stiffness constant, the actuator stiffness k_a is decreased when k_p is increased ($k_a = k_n - k_p$, with k_n the total nano-hexapod stiffness). A high-pass filter is also added to limit the low-frequency gain with a cut-off frequency ω_i equal to one tenth of the system resonance ($\omega_i = \omega_0/10$).

The achievable maximum simultaneous damping of all the modes is computed as a function of the parallel stiffnesses (Figure 7.3). It is shown that the soft nano-hexapod cannot yield good damping because the parallel stiffness cannot be sufficiently large compared to the negative stiffness induced by the rotation. For the two stiff options, the achievable damping decreases when the parallel stiffness is too high, as explained in Section 4. Such behavior can be explained by the fact that the achievable damping can be approximated by the distance between the open-loop pole and the open-loop zero [16, chapt 7.2]. This distance is larger for stiff nano-hexapod because the open-loop pole will be at higher frequencies while the open-loop zero, whereas depends on the value of the parallel stiffness, can only be made large for stiff nano-hexapods.

Let's choose $k_p = 1\,N/mm$, $k_p = 0.01\,N/\mu m$ and $k_p = 1\,N/\mu m$ for the three considered nano-hexapods. The corresponding optimal controller gains and achievable damping are summarized in Table 7.2.

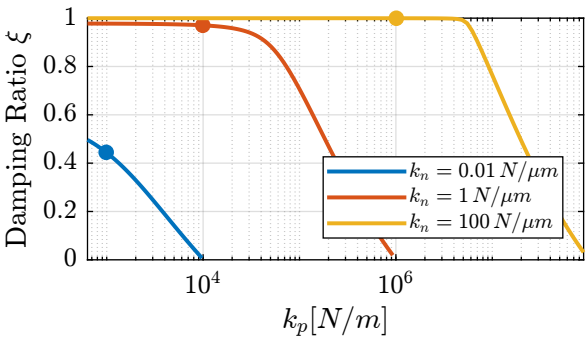

Figure 7.3: Maximum damping ξ as a function of the parallel stiffness k_p

Table 7.2: Obtained optimal parameters for the IFF controller when using parallel stiffnesses

k_n	k_p	g	ξ_{opt}
$0.01\,N/\mu m$	$1\,N/mm$	47.9	0.44
$1\,N/\mu m$	$0.01\,N/\mu m$	465.57	0.97
$100\,N/\mu m$	$1\,N/\mu m$	4624.25	0.99

7.4 Optimal Relative Motion Control

For each considered nano-hexapod stiffness, relative damping control is applied and the achievable damping ratio as a function of the controller gain is computed (Figure 7.4). The gain is chosen such that 99% of modal damping is obtained (obtained gains are summarized in Table 7.3).

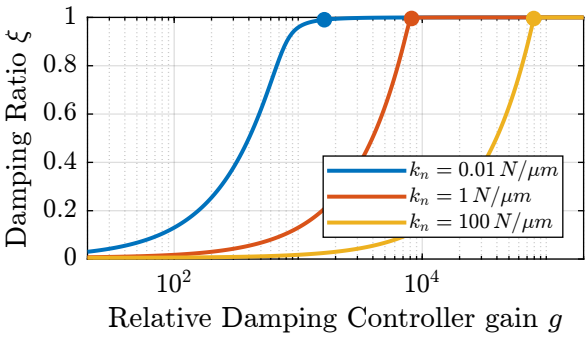

Figure 7.4: Maximum damping ξ as a function of the RDC gain g

Table 7.3: Obtained optimal parameters for the RDC

k_n	g	ξ_{opt}
$0.01\,N/\mu m$	1600	0.99
$1\,N/\mu m$	8200	0.99
$100\,N/\mu m$	80000	0.99

7.5 Comparison of the obtained damped plants

Now that the optimal parameters for the three considered active damping techniques have been determined, the obtained damped plants are computed and compared in Figure 7.5.

Similar to what was concluded in the previous analysis:

- IFF adds more coupling below the resonance frequency as compared to the open-loop and RDC cases
- All three methods yield good damping, except for IFF applied on the soft nano-hexapod
- Coupling is smaller for stiff nano-hexapods

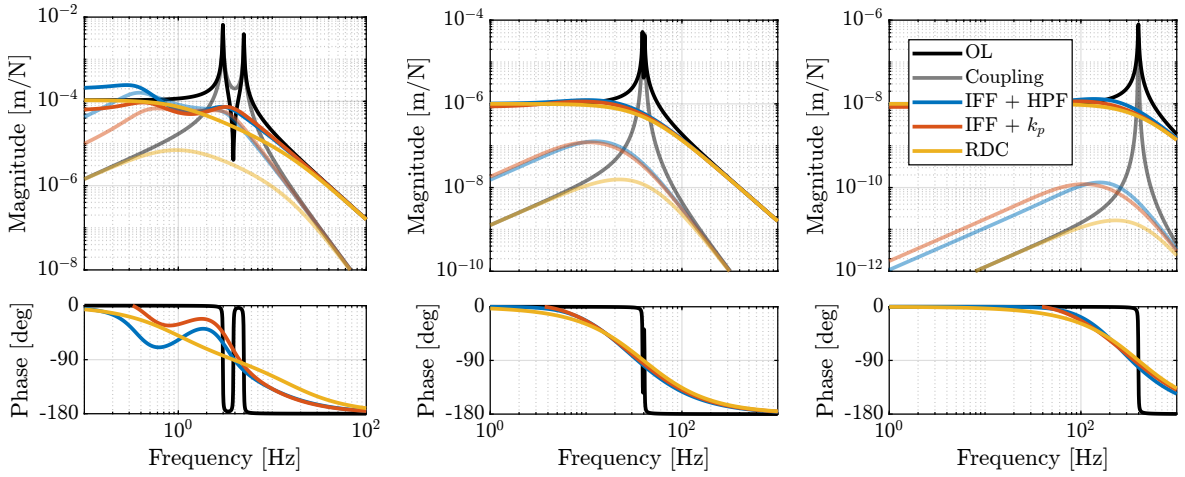

(a) $k_n = 0.01\,N/\mu m$ **(b)** $k_n = 1\,N/\mu m$ **(c)** $k_n = 100\,N/\mu m$

Figure 7.5: Comparison of the damped plants for the three proposed active damping techniques (IFF with HPF in blue, IFF with k_p in red and RDC in yellow). The direct terms are shown by solid lines, and the coupling terms are shown by the shaded lines. Three nano-hexapod stiffnesses are considered. For this analysis the rotating velocity is $\Omega = 60\,\text{rpm}$ and the suspended mass is $m_n + m_s = 16\,\text{kg}$.

8 Nano-Active-Stabilization-System with rotation

Until now, the model used to study gyroscopic effects consisted of an infinitely stiff rotating stage with a X-Y suspended stage on top. While quite simplistic, this allowed us to study the effects of rotation and the associated limitations when active damping is to be applied. In this section, the limited compliance of the micro-station is considered as well as the rotation of the spindle.

8.1 Nano Active Stabilization System model

To have a more realistic dynamics model of the NASS, the 2-DoF nano-hexapod (modeled as shown in Figure 1.1) is now located on top of a model of the micro-station including (see Figure 8.1 for a 3D view):

- the floor whose motion is imposed
- a 2-DoF granite ($k_{g,x} = k_{g,y} = 950\,\text{N}/\mu\text{m}$, $m_g = 2500\,\text{kg}$)
- a 2-DoF T_y stage ($k_{t,x} = k_{t,y} = 520\,\text{N}/\mu\text{m}$, $m_t = 600\,\text{kg}$)
- a spindle (vertical rotation) stage whose rotation is imposed ($m_s = 600\,\text{kg}$)
- a 2-DoF micro-hexapod ($k_{h,x} = k_{h,y} = 61\,\text{N}/\mu\text{m}$, $m_h = 15\,\text{kg}$)

A payload is rigidly fixed to the nano-hexapod and the x, y motion of the payload is measured with respect to the granite.

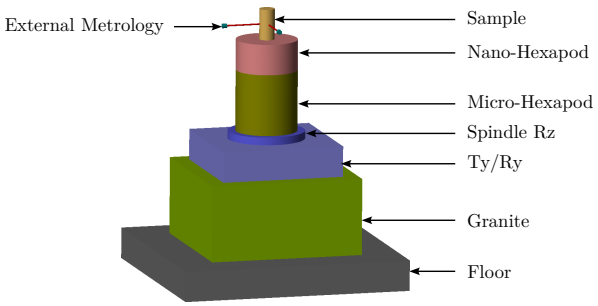

Figure 8.1: 3D view of the Nano-Active-Stabilization-System model.

8.2 System dynamics

The dynamics of the undamped and damped plants are identified using the optimal parameters found in Section 7. The obtained dynamics are compared in Figure 8.2 in which the direct terms are shown by the solid curves and the coupling terms are shown by the shaded ones. It can be observed that:

- The coupling (quantified by the ratio between the off-diagonal and direct terms) is higher for the soft nano-hexapod
- Damping added using the three proposed techniques is quite high, and the obtained plant is rather easy to control
- There is some coupling between nano-hexapod and micro-station dynamics for the stiff nano-hexapod (mode at 200Hz)
- The two proposed IFF modifications yield similar results

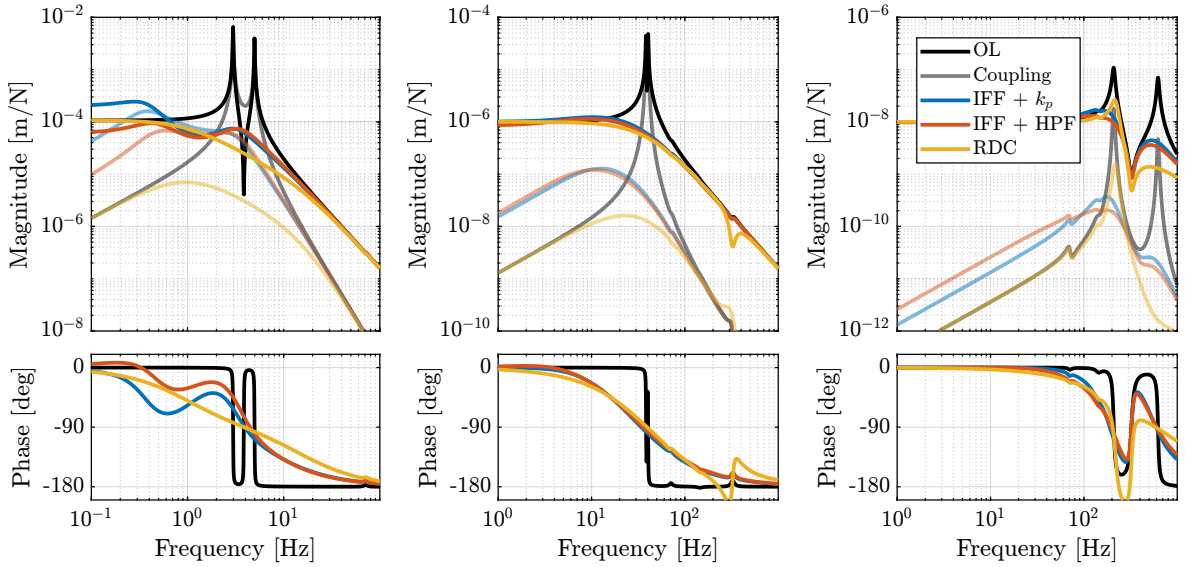

(a) $k_n = 0.01\,N/\mu m$ **(b)** $k_n = 1\,N/\mu m$ **(c)** $k_n = 100\,N/\mu m$

Figure 8.2: Bode plot of the transfer function from nano-hexapod actuator to measured motion by the external metrology

8.3 Effect of disturbances

The effect of three disturbances are considered (as for the uniaxial model), floor motion $[x_{f,x},\ x_{f,y}]$ (Figure 8.3), micro-Station vibrations $[f_{t,x},\ f_{t,y}]$ (Figure 8.4) and direct forces applied on the sample $[f_{s,x},\ f_{s,y}]$ (Figure 8.5). Note that only the transfer functions from the disturbances in the x direction to the relative position d_x between the sample and the granite in the x direction are displayed because the transfer functions in the y direction are the same due to the system symmetry.

Conclusions are similar than those of the uniaxial (non-rotating) model:

- Regarding the effect of floor motion and forces applied on the payload:
  - The stiffer, the better. This can be seen in Figures 8.3 and 8.5 where the magnitudes for the stiff hexapod are lower than those for the soft one
  - IFF degrades the performance at low-frequency compared to RDC
- Regarding the effect of micro-station vibrations:
  - Having a soft nano-hexapod allows filtering of these vibrations between the suspension modes of the nano-hexapod and some flexible modes of the micro-station. Using relative damping control reduces this filtering (Figure 8.4a).

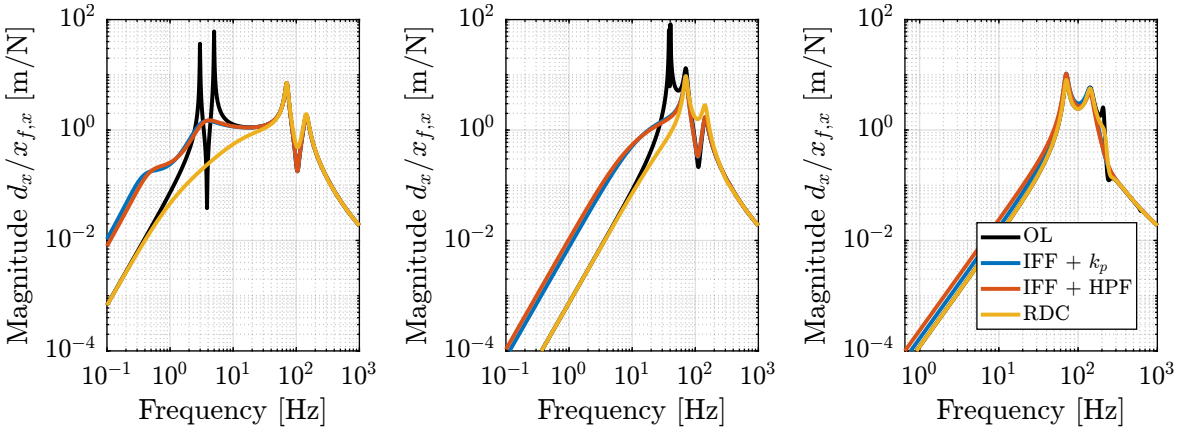

(a) $k_n = 0.01\,N/\mu m$ **(b)** $k_n = 1\,N/\mu m$ **(c)** $k_n = 100\,N/\mu m$

Figure 8.3: Effect of floor motion $x_{f,x}$ on the position error d_x - Comparison of active damping techniques for the three nano-hexapod stiffnesses. IFF is shown to increase the sensitivity to floor motion at low-frequency.

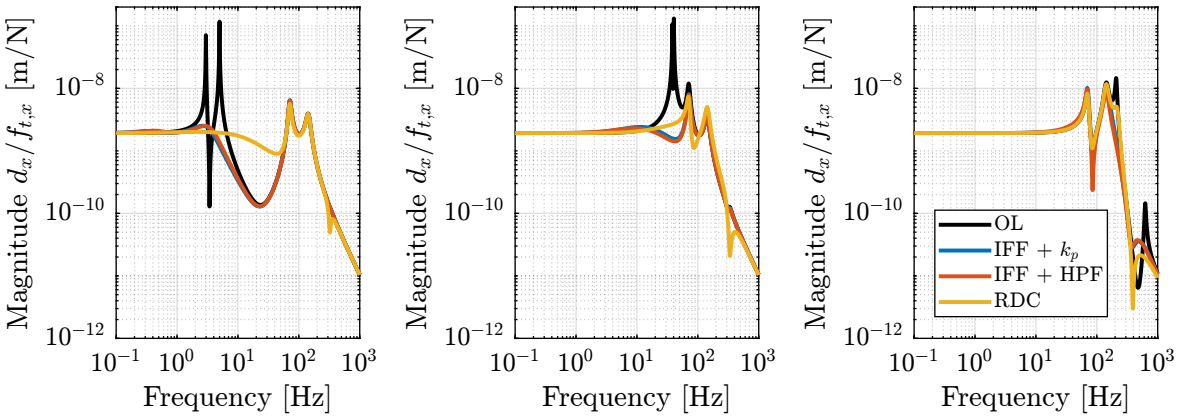

(a) $k_n = 0.01\,N/\mu m$ **(b)** $k_n = 1\,N/\mu m$ **(c)** $k_n = 100\,N/\mu m$

Figure 8.4: Effect of micro-station vibrations $f_{t,x}$ on the position error d_x - Comparison of active damping techniques for the three nano-hexapod stiffnesses. Relative Damping Control increases the sensitivity to micro-station vibrations between the soft nano-hexapod suspension modes and the micro-station modes (a)

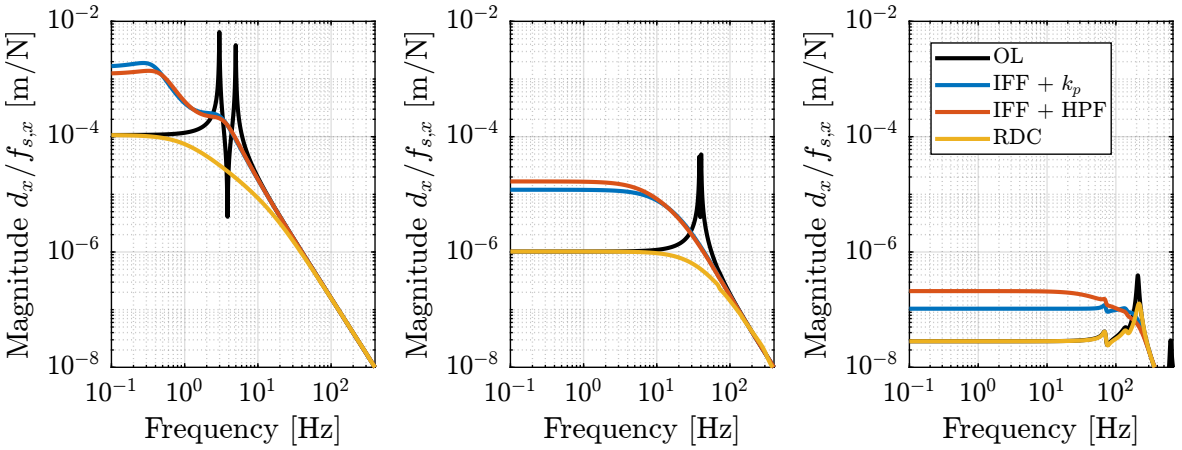

(a) $k_n = 0.01\,N/\mu m$ **(b)** $k_n = 1\,N/\mu m$ **(c)** $k_n = 100\,N/\mu m$

Figure 8.5: Effect of sample forces $f_{s,x}$ on the position error d_x - Comparison of active damping techniques for the three nano-hexapod stiffnesses. Integral Force Feedback degrades this compliance at low-frequency.

Conclusion

In this study, the gyroscopic effects induced by the spindle's rotation have been studied using a simplified model (Section 1). Decentralized Integral Force Feedback with pure integrators was shown to be unstable when applied to rotating platforms (Section 2). Two modifications of the classical IFF control have been proposed to overcome this issue.

The first modification concerns the controller and consists of adding a high-pass filter to the pure integrators. This is equivalent to moving the controller pole to the left along the real axis. This allows the closed-loop system to be stable up to some value of the controller gain (Section 3).

The second proposed modification concerns the mechanical system. Additional springs are added in parallel with the actuators and force sensors. It was shown that if the stiffness k_p of the additional springs is larger than the negative stiffness $m\Omega^2$ induced by centrifugal forces, the classical decentralized IFF regains its unconditional stability property (Section 4).

These two modifications were compared with Relative Damping Control in Section 6. While having very different implementations, both proposed modifications were found to be very similar with respect to the attainable damping and the obtained closed-loop system behavior.

This study has been applied to a rotating platform that corresponds to the nano-hexapod parameters (Section 7). As for the uniaxial model, three nano-hexapod stiffnesses values were considered. The dynamics of the soft nano-hexapod ($k_n = 0.01\,N/\mu m$) was shown to be more depend more on the rotation velocity (higher coupling and change of dynamics due to gyroscopic effects). In addition, the attainable damping ratio of the soft nano-hexapod when using IFF is limited by gyroscopic effects.

To be closer to the Nano Active Stabilization System dynamics, the limited compliance of the micro-station has been considered (Section 8). Results are similar to those of the uniaxial model except that come complexity is added for the soft nano-hexapod due to the spindle's rotation. For the moderately stiff nano-hexapod ($k_n = 1\,N/\mu m$), the gyroscopic effects only slightly affect the system dynamics, and therefore could represent a good alternative to the soft nano-hexapod that showed better results with the uniaxial model.

Bibliography

[1] T. Dehaeze and C. Collette, "Active damping of rotating platforms using integral force feedback," in *Proceedings of the International Conference on Modal Analysis Noise and Vibration Engineering (ISMA)*, 2020.

[2] T. Dehaeze and C. Collette, "Active damping of rotating platforms using integral force feedback," *Engineering Research Express*, Feb. 2021.

[3] C. Collette, S. Janssens, and K. Artoos, "Review of active vibration isolation strategies," *Recent Patents on Mechanical Engineeringe*, vol. 4, no. 3, pp. 212–219, 2011 (cit. on p. 8).

[4] H. Lin and J. E. McInroy, "Disturbance attenuation in precise hexapod pointing using positive force feedback," *Control Engineering Practice*, vol. 14, no. 11, pp. 1377–1386, 2006.

[5] J. Fanson and T. K. Caughey, "Positive position feedback control for large space structures," *AIAA journal*, vol. 28, no. 4, pp. 717–724, 1990.

[6] A. Preumont, J.-P. Dufour, and C. Malekian, "Active damping by a local force feedback with piezoelectric actuators," in *32nd Structures, Structural Dynamics, and Materials Conference*, American Institute of Aeronautics and Astronautics, Apr. 1991 (cit. on pp. 8, 11).

[7] D. Karnopp, M. J. Crosby, and R. Harwood, "Vibration control using semi-active force generators," *Journal of Engineering for Industry*, vol. 96, pp. 619–626, 1974.

[8] M. Serrand and S. Elliott, "Multichannel feedback control for the isolation of base-excited vibration," *Journal of Sound and Vibration*, vol. 234, no. 4, pp. 681–704, 2000.

[9] A. Preumont, A. François, F. Bossens, and A. Abu-Hanieh, "Force feedback versus acceleration feedback in active vibration isolation," *Journal of Sound and Vibration*, vol. 257, no. 4, pp. 605–613, 2002 (cit. on p. 8).

[10] A. Preumont, B. De Marneffe, and S. Krenk, "Transmission zeros in structural control with collocated multi-input/multi-output pairs," *Journal of guidance, control, and dynamics*, vol. 31, no. 2, pp. 428–432, 2008 (cit. on p. 8).

[11] Y. R. Teo and A. J. Fleming, "Optimal integral force feedback for active vibration control," *Journal of Sound and Vibration*, vol. 356, pp. 20–33, Nov. 2015 (cit. on p. 8).

[12] S. Chesné, A. Milhomem, and C. Collette, "Enhanced damping of flexible structures using force feedback," *Journal of Guidance, Control, and Dynamics*, vol. 39, no. 7, pp. 1654–1658, 2016 (cit. on p. 8).

[13] G. Zhao, A. Paknejad, A. Deraemaeker, and C. Collette, "$\mathcal{H}_\infty$ optimization of an integral force feedback controller," *Journal of Vibration and Control*, vol. 25, no. 17, pp. 2330–2339, 2019 (cit. on p. 8).

[14] S. Skogestad and I. Postlethwaite, *Multivariable Feedback Control: Analysis and Design - Second Edition*. John Wiley, 2007.

[15] B. de Marneffe, "Active and passive vibration isolation and damping via shunted transducers," Ph.D. dissertation, Université Libre de Bruxelles, Brussels, Belgium, 2007.

[16] A. Preumont, *Vibration Control of Active Structures - Fourth Edition* (Solid Mechanics and Its Applications). Springer International Publishing, 2018 (cit. on pp. 17, 26).

Acronyms

Notation	Description
HPF	high-pass filter
IFF	Integral Force Feedback
NASS	Nano Active Stabilization System
RDC	Relative Damping Control